ACS Catalysis

Research Article

Cite This: ACS Catal. 2018, 8, 4120−4131

pubs.acs.org/acscatalysis

Identifying Dynamic Structural Changes of Active Sites in Pt−Ni Bimetallic Catalysts Using Multimodal Approaches

Deyu Liu,[†,○] Yuanyuan Li,[‡,○] Matthew Kottwitz,[†] Binhang Yan,[§] Siyu Yao,[§] Andrew Gamalski,[⊥] Daniel Grolimund,[∥] Olga V. Safonova,[∥] Maarten Nachtegaal,[∥] Jingguang G. Chen,[*,§,#] Eric A. Stach,[*,⊥,▽] Ralph G. Nuzzo,[*,†] and Anatoly I. Frenkel[*,‡,§]

[†]Department of Chemistry, University of Illinois, Urbana, Illinois 61801, United States

[‡]Department of Materials Science and Chemical Engineering, Stony Brook University, Stony Brook, New York 11794, United States

[§]Division of Chemistry, Brookhaven National Laboratory, Upton, New York 11973, United States

[∥]Paul Scherrer Institute, 5232 Villigen, Switzerland

[⊥]Center for Functional Nanomaterials, Brookhaven National Laboratory, Upton, New York 11973, United States

[#]Department of Chemical Engineering, Columbia University, New York, New York 10027, United States

[▽]Department of Materials Science and Engineering, University of Pennsylvania, Philadelphia, Pennsylvania 19104, United States

Supporting Information

ABSTRACT: Alloy nanoparticle catalysts are known to afford unique activities that can differ markedly from their parent metals, but there remains a generally limited understanding of the nature of their atomic (and likely dynamic) structures as exist in heterogeneously supported forms under reaction conditions. Notably unclear is the nature of their active sites and the details of the varying oxidation states and atomic arrangements of the catalytic components during chemical reactions. In this work, we describe multimodal methods that provide a quantitative characterization of the complex heterogeneity present in the chemical and electronic speciations of Pt−Ni bimetallic catalysts supported on mesoporous silica during the reverse water gas shift reaction. The analytical protocols involved a correlated use of in situ X-ray Absorption Spectroscopy (XAS) and Diffuse Reflectance Infrared Fourier Transform Spectroscopy (DRIFTS), complimented by ex-situ aberration corrected Scanning Transmission Electron Microscopy (STEM). The data reveal that complex reactions occur between the metals and support in this system under operando conditions. These reactions, and the specific impacts of strong metal−silica bonding interactions, prevent the formation of alloy phases containing Ni−Ni bonds. This feature of structure provides high activity and selectivity for the reduction of CO_2 to carbon monoxide without significant competitive levels of methanation. We show how these chemistries evolve to the active state of the catalyst: bimetallic nanoparticles possessing an intermetallic structure (the active phase) that are conjoined with Ni-rich, metal-silicate species.

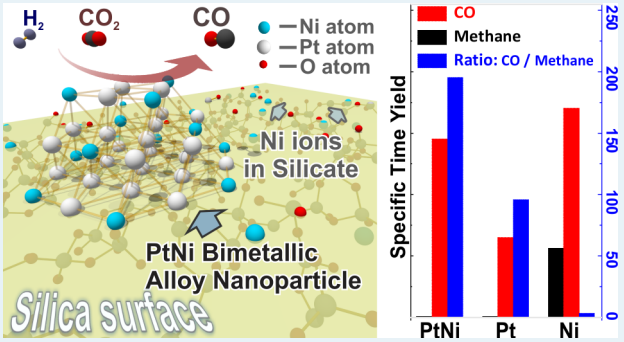

KEYWORDS: *bimetallic nanoparticles, catalysis, platinum, nickel, reverse water gas shift, STEM, XAS, DRIFTS*

INTRODUCTION

Supported alloy nanoparticle (NP) catalysts have been widely used for heterogeneous catalysis, with applications in reforming processes, selective hydrogenation/oxidation, and other important reactions in both the petroleum and fine chemical industries.[1−4] After decades of research and development, candidate components can be rationally selected, at least partially, based on theoretical predictions of electronic structure, adsorption properties, and mechanisms of catalysis.[5−7] In many cases, understanding the structures adopted by supported metal NPs in the environments of their use can provide a key to understanding their catalytic properties. It is now well appreciated that supported NPs can differ from their bulk counterparts in significant ways affecting catalytic performance. These include the presence of a high density of low coordination number sites, surface relaxation and other forms of bond strain, as well as the effects of quantum confinement on electronic structure. Perhaps most notably, very small metal NPs are stabilized by poorly understood bonding interactions with their supports, which can lead to changes in their physical and chemical behaviors.[8,9] The current work examines such a system and documents a set of multimodal characterization tools that serve to illuminate the nature of the complex speciations present in bimetallic Pt−Ni

Received: February 20, 2018
Revised: April 1, 2018
Published: April 2, 2018

DOI: 10.1021/acscatal.8b00706
ACS Catal. 2018, 8, 4120−4131

catalysts supported on mesoporous silica during the reverse water gas shift reaction.

Many supported metals have been studied as catalysts for the water gas (WGS) and reverse water gas (rWGS) shift reactions, processes used in steam reforming and Fischer−Tropsch processes to adjust H_2/CO ratios in syngas.[10−12] The catalyzed conversion of CO_2 to CO has also been recognized as a potential method for the chemical fixation of CO_2 released from fossil fuel combustion. For instance, CO is a carbon source for industrial production of long-chain hydrocarbons via the Fischer−Tropsch process.[13] Along with the production of CO, CH_4 can be generated as a significant byproduct of CO_2 hydrogenation (via further hydrogenation of CO), although with a lower market value than CO at present.[14] The hydrogenation of CO_2 to CO and the hydrogenation of CO into multiple byproducts (primarily methane) are all commonly catalyzed by transition metals, with pathways that share multiple elementary steps.[14,15] Additionally—because these processes have a similar activation energy—CO and CH_4 are often produced from CO_2.[15−17] Although CH_4 is of higher market value than CO_2, a reaction that leads to the creation of a mixture of CO and CH_4 is much less useful since these molecules are most generally utilized as inputs for different subsequent processes (except in the case of combustion). Therefore, the structural study of an exemplary system with enhanced selectivity for CO is of great importance. Compared to monometallic NPs, alloy NPs exhibit greater tunability of their surface structure and electronic properties, which makes it possible to differentiate between reaction pathways to achieve a higher activity and improved selectivity.

Given the critical correlation between structure and catalytic properties, the preparation of supported metal catalysts needs to be optimized to achieve the desired size, composition, spatial distribution, morphology, and interfaces as well as provide capacities for regeneration and long lifetimes on stream. In addition to chemical reactions that can impact the composition of a metal catalyst (e.g., poisoning), the valence states, atomic arrangements, and even metal-particle sizes can be significantly affected by the chemical environments present under working conditions.[18−20] For instance, the surface segregation and surface chemistry of alloy NPs are determined not only by the intrinsic properties of the components in the alloy but are also affected by species adsorbing from the ambient reaction.[21] These effects can lead to the specific segregation of alloy constituents,[19,22] as well as reconstructions that impact the nature and numbers of active surface sites.[23,24] The nature of this complexity motivates the development of new multimodal methods suited to characterize such features in catalysts both in situ and in their working conditions (operando)—to provide fully established understandings of structure−property correlations in catalysis.[18−20,22] A study of catalysts following this concept needs to combine not only typical structural characterization techniques but also specially designed protocols to extract information regarding dynamical/compositional attributes of structural evolution induced by changes in operando chemical environments.

The finite cluster sizes of supported nanoscale bimetallic catalysts provide a point of particular interest here as they provide perturbations that in some cases can preclude the formation of known bulk alloy/intermetallic phases, but instead drive the adoption of new and even highly disordered structures. A goal of the present work is to study how support effects, and more specifically solid−solid reactions occurring with it, can both drive and stabilize the formation of intermetallic phases in supported NP catalysts. We describe the operando structural dynamics seen during the rWGS reaction catalyzed by a bimetallic PtNi catalyst supported on the mesoporous silica, SBA-15. The known high activity of the PtNi bimetallic system in this case is found to act in synergy with the mesoporous silica, which (as we will show) strongly stabilizes the formation of very small bimetallic (and likely intermetallic) particles conjoined with a dispersed Ni-silicate phase as required to preserve mass balance.[25−27] The data from this multimodal study reveal a complex interplay of thermochemical−kinetic features that mediate the temporal and compositional evolution of operando structure in this bimetallic catalyst.

We present below the results of a multimodal operando study of the hydrogenation of CO_2, highlighting a unit stoichiometry (1:1) nanoscale PtNi catalyst supported on mesoporous silica (PtNi/SBA-15). The work specifically focuses on the structure (spatial/atomic and electronic)−performance relationships of the metals as present in their most active form. These catalysts show both high activities and selectivity for the rWGS reaction over a broad range of operando conditions, producing CO from the partial hydrogenation of CO_2 without significant levels of over reduction to methane. The large penetration depth of the hard X-rays used in this work (X-ray Absorption Spectroscopy) provides a means to fully speciate the complex (and, as we show, compositionally/structurally heterogeneous) operando bonding of the metals present both on and within the pores of the SBA-15. We adopted a previously described multiprobe microreactor platform[28] to carry out the X-ray Absorption Fine Structure (XAFS) studies in this work and provide a means to meaningfully correlate those results with data from other methods—a combination of in situ micro-XAFS complimented by ex situ Scanning Transmission Electron Microscopy (STEM) and further correlated with kinetics and product conversion measurements made by online Gas Chromatography−Mass Spectrometry (GC-MS) and metal−adsorbate bonding. The latter are deduced via *in situ* Diffuse Reflectance Infrared Fourier Transform Spectroscopy (DRIFTS). Taken together, the data reveal a compositional/structural model for the operando catalyst that embeds both nanoscale Ni-silicate and PtNi alloy (likely intermetallic) phases. The strong (and in this case Ni-reactive) metal−support interactions drive the formation of an off-stoichiometry (Pt-rich) intermetallic phase that eliminates in-operando homometallic Ni−Ni interactions in favor of heterometallic Pt−Ni bonding and serves as the active phase for the selective reduction of CO_2.

EXPERIMENTAL SECTION

Chemicals and Materials. Ultrapure water (18.2 M·Ohm) from a Millipore purification system was used throughout this work. SBA-15 mesoporous silica was purchased from ACS materials. $Ni(NO_3)_2{\cdot}6H_2O$ (99%, Acros) and $[Pt(NH_3)_4]Cl_2{\cdot}xH_2O$ (98%) were purchased from Sigma-Aldrich; ammonia hydroxide (28−30%) was purchased from Fisher Scientific.

Preparation of Supported Catalysts. In a typical preparation process, 0.50 g of SBA-15 mesoporous silica was dispersed in 8 mL of 0.6% $NH_3{\cdot}H_2O$ aqueous solution by sonication for 1 h. Afterward, metal precursors dissolved as 4 mL of aqueous solution was added to the aforementioned SBA-15 dispersion. For a loading of 1:1 Ni/Pt atomic ratio (with ca. 1 wt % Pt normalized to silica), the precursor solution was

DOI: 10.1021/acscatal.8b00706
ACS Catal. 2018, 8, 4120−4131

prepared as follows: Nickel was converted into $[Ni(NH_3)_6]^{2+}$, by dissolving 7.5 mg of $Ni(NO_3)_2{\cdot}6H_2O$ in 1.5 mL of H_2O followed by 0.1 mL of 30% $NH_3{\cdot}H_2O$ solution, then 8.5 mg of $[Pt(NH_3)_4]Cl_2{\cdot}xH_2O$ ($x \approx 2$) was added to the solution and diluted to 4 mL. After adding the precursor solution, the SBA-15 dispersion was left under stirring for 4 h. The loaded silica was separated and washed by centrifuge/redispersing for four cycles in water to remove ammonia and anions from precursors. After drying overnight at 358 K, the sample was crushed into a powder, calcined at 573 K in the air for 2 h (1 K/min heating ramp), and reduced in 5% H_2 at 673 K for 2 h (5 K/min). The same procedure was used for monometallic loading, except only one precursor was used with a doubled amount to achieve the same total molar loading of metal. The metal compositions were confirmed by ICP elemental analyses that affirmed loading efficiencies of 90−100% (the measured wt % loadings of Ni and Pt were 0.32% and 0.93%, respectively, in the bimetallic catalyst and 0.63% and 1.83% in the corresponding monometallic catalysts).

Scanning Transmission Electron Microscopy Characterization. High-angle annular dark-field−scanning transmission electron microscopy (HAADF-STEM) was used to measure the size distribution of the particles. The sample was suspended in water and drop-casted onto lacey carbon copper grids (Ted Pella) for analysis using a JEOL 2200-FS TEM operated at 200 kV in STEM mode. STEM-Energy Dispersive X-ray analysis (EDX) mapping was performed in the Center for Functional Nanomaterials at Brookhaven National Laboratory with an FEI Talos F200X TEM (operated at 200 keV) equipped with an energy dispersive X-ray spectrometer.

XAFS Experiments. X-ray absorption fine structure data were collected at the microXAS beamline (μ-XAS, X05LA) of the Swiss Light Source (SLS), Paul Scherrer Institute. Measurements were performed with a microreactor[28,29] in fluorescence mode with the incident pencil beam focused by a Kirkpatrick−Baez (KB) mirror system to the size of 30 × 10 (H × V) μm^2. The incident X-ray intensity was monitored by a mini ion chamber continuously flushed with N_2, and the fluorescence signal was monitored by a Silicon Drift Detector. Detailed data processing and a fitting procedure are included in the Supporting Information (SI), section 5. For the operando measurements, the sample was treated using the following sequence: (1) activation in 5% H_2 at 673 K for 2 h; (2) r-WGS reaction conditions of 10% CO_2 and 20% H_2 at 673 K for 2 h; (3) full oxidation in 20% O_2 at 673 K for 2 h. The microreactor was operated with a release valve that constrained the pressure at 1 atm. The flow rate was 0.2 sccm through the cell. A quadrupole mass spectrometer (Hiden) was used to monitor the integrity and gas composition in the microcell.

DRIFTS Experiments. The spectra were collected using a Nicolet 6700 FTIR spectrometer equipped with a rapid-scanning liquid-nitrogen-cooled mercury cadmium telluride (MCT) detector and a Harrick reaction chamber.[30] Before each measurement, the catalyst was pretreated in a 20 mL/min 25% H_2/He mixture at 673 K for 1 h and then purged with 20 mL/min He for 20 min. Subsequently, the catalyst was cooled to room temperature, and the corresponding background spectrum (512 scans) was acquired with a resolution of 4 cm^{-1}. The DRIFT spectra featuring CO adsorption were recorded after the samples were exposed to CO (5 mL/min CO balanced with 15 mL/min He) at room temperature for 30 min and the purging of a helium flow at 20 mL/min for 30 min. The DRIFT spectra shown in this work were expressed in units of Kubelka−Munk absorbance.

Flow Reactor Test. Flow reactor studies of the CO_2 hydrogenation reaction were performed in a 1/4 in. quartz tube reactor under atmospheric pressure. Approximately 50 mg of sieved catalysts (40−60 mesh) were used for steady-state experiments. H_2 and CO_2 were set at a 2:1 ratio (10 mL/min H_2 with 5 mL/min CO_2) and diluted with 25 mL/min Ar. Prior to each test, the catalyst was first reduced at 673 K for 60 min in a H_2/Ar mixture (10 mL/min H_2 and 30 mL/min Ar). Then, the inlet flow was switched to reactants and held for at least 14 h. After the steady-state measurement, the reaction temperature was changed from 673 to 613 K in 10 K increments so that the effect of temperature on the reaction rate of CO_2 and H_2 could be studied. The concentrations of gas products were analyzed online by a gas chromatography instrument (Agilent 7890B) equipped with a flame ionization detector (FID) and a thermal conductivity detector (TCD).

Pulse CO Chemisorption Measurements. Pulse CO chemisorption measurements were performed on an AMI-300ip (Altamira) instrument. Approximately 20 mg of catalyst was loaded into a U-shaped quartz tube and dried at 393 K with 30 mL/min He for 30 min. The reduction was performed in a 30 sccm 10% H_2/Ar flow, with a heating rate of 10 K/min from 323 to 723 K and then held at 723 K for 45 min (since the reactor is much larger than the microcell, we used a slightly higher temperature to ensure the complete/equilibrated reduction of the metal loadings). The reduced sample was then purged in 30 mL/min He for 20 min for degassing at 723 K and cooled to 313 K. Pulses of 10% CO balanced with He (loop 590 μL) were injected onto a 50 mL/min He stream until the peak area became constant. The amount of CO flowing out of the reactor was analyzed by a thermal conductivity detector (TCD).

RESULTS AND DISCUSSION

It is now well appreciated that supported bimetallic catalysts can offer marked advantages with regard to important process-centric metrics that include activity, selectivity, and stability on stream.[31−34] The current literature describes many procedures for the synthesis of supported catalysts of this form (e.g., impregnation by incipient wetness etc.[35]), and there remains a broad interest in the development of new methods that can provide improvements regarding the forms of heterogeneity (e.g., in terms of the compositional and size distributions) these materials embed. The characterization of systems in which such forms of complexity are prominent remains a significant challenge and helps motivate current interests related to the development of new multimodal operando methodologies.[36] Such methods are exploited in the current work, which examines a new variant of a widely studied bimetallic catalyst composition for the rWGS reaction— nanoscale (~1 nm) PtNi catalysts supported on mesoporous silica (PtNi/SBA-15). These methods illustrate that an unexpected form of compositional/structural heterogeneity characterizes the operando structure of these catalyst materials and establish a precise speciation of the active phase that affords high rate and high selectivity conversions.

To prepare the supported catalysts examined in this work, we used a cation-exchange method to promote dispersion of the metal precursors on the support.[37−40] To this end, we chose mesoporous SBA-15 silica as a support because it provides a charged surface for cation exchange and a high specific surface

DOI: 10.1021/acscatal.8b00706
ACS Catal. 2018, 8, 4120−4131

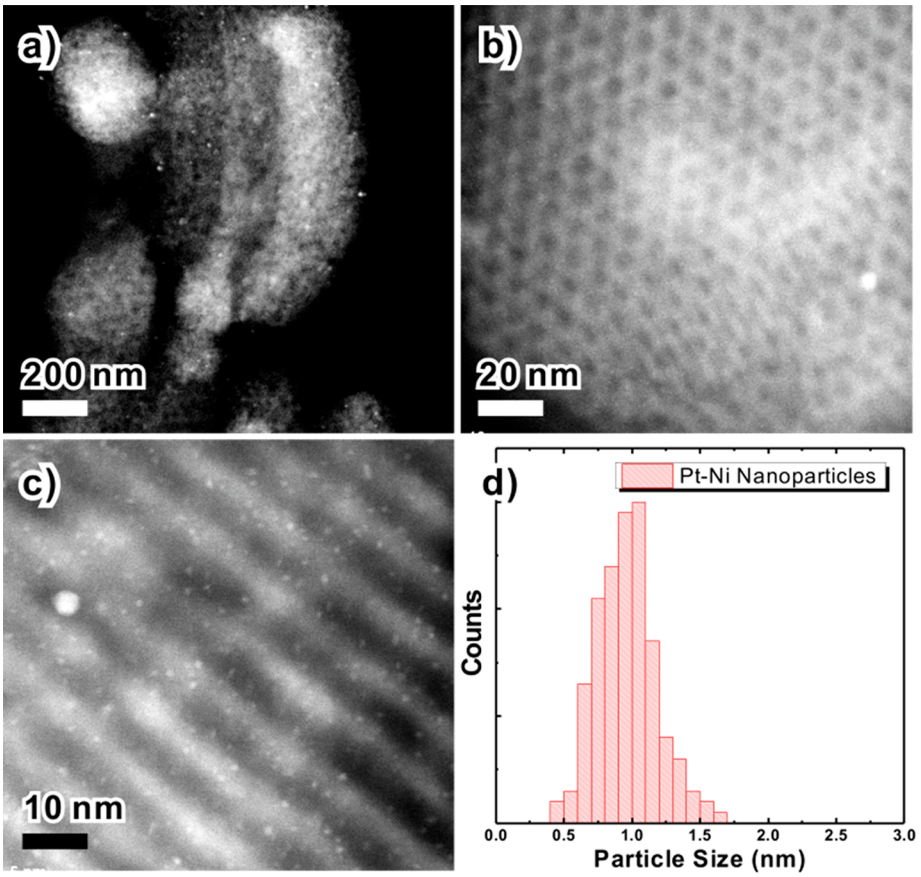

Figure 1. Scanning transmission electron micrograph of (a) micrometer-scale general view of the bimetallic loaded SBA-15 support. (b) Channel-end and (c) -side view of the PtNi/SBA-15 catalyst under different magnifications and (d) the histogram of particle size for observed clusters (200 counts), showing a narrow distribution centered at 0.95 nm. The micrographs demonstrate the uniform spatial and size distribution of supported NPs. Note that the significantly larger particles (~5 nm) with a very small population are excluded from the histogram.

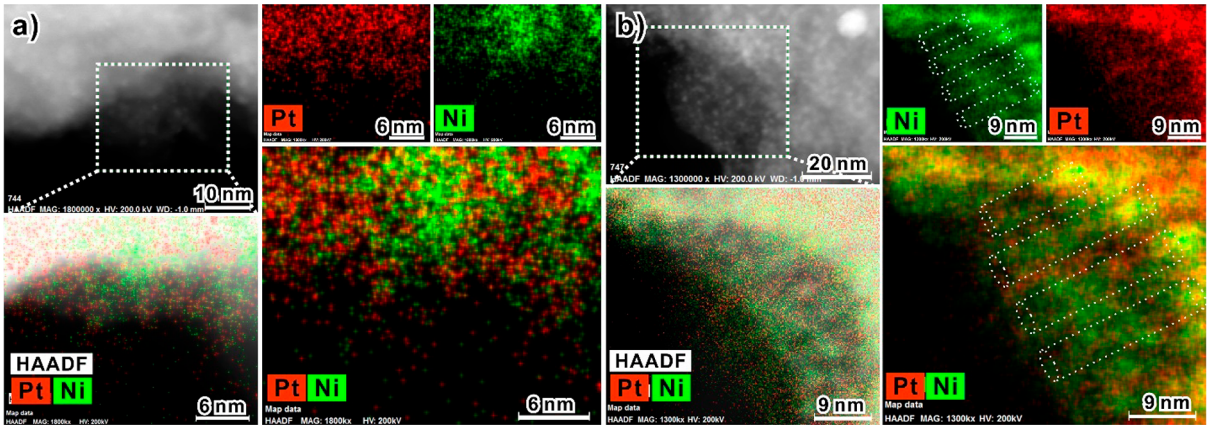

Figure 2. HAADF-STEM images and EDX maps showing the distribution of Ni and Pt in the PtNi/SBA-15 catalyst. We find two typical morphologies: in a, the Pt and Ni are distributed over the support, with some local clustering observed; in b, there is evidence that the Ni distribution is segregated within the pores of the SBA-15 support, as evidenced by both the alignment and spacing of the Ni distribution.

area (>600 m^2/g) sufficient to carry metal contents as high as 8−10% for both Ni and Pt while retaining small particle sizes and resistance to sintering on reduction.[41,42] The details of the synthesis and catalyst activation procedures are given in the Experimental Section.

The nature of the metal species obtained after the final reduction step at 673 K was examined by STEM, where images show an extensive dispersion of small bimetallic PtNi clusters (vide infra) throughout the SBA-15 support (Figure 1a−c). Quantitative analyses of the microscopy data show a uniform morphology with a narrow distribution of particles 0.96 ± 0.22 nm in diameter distributed throughout the pores (Figure 1d). Additionally, there were very few (less than 1 count per several pore channels) larger particles (~5 nm), a number sufficiently small so as to contribute negligibly to the catalytic performance. As will be discussed later, the average size of the PtNi NPs deduced from operando XAS data is about 1 nm (ensembles of about 37 atoms), which agrees well with the STEM results. In

DOI: 10.1021/acscatal.8b00706
ACS Catal. 2018, 8, 4120−4131

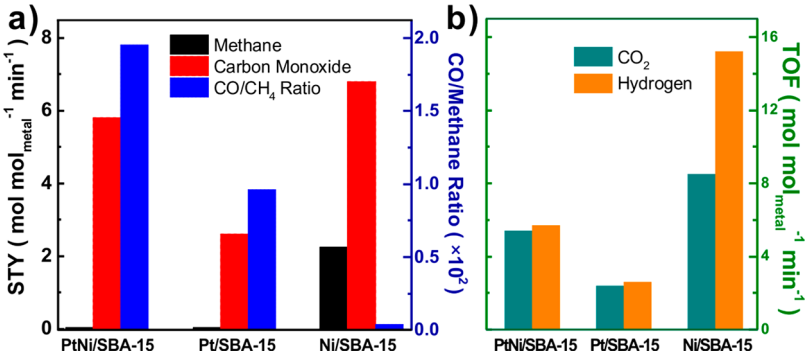

Figure 3. Characteristic catalytic performance of metal/SBA-15 catalysts in the flow reactor test of rWGS reaction at 673 K: (a) Specific Time Yields (STY) of CO and CH_4 over PtNi/SBA-15, Pt/SBA-15, and Ni/SBA-15, respectively; the bimetallic catalyst shows good activity and very high selectivity (described by the CO/CH_4 molar ratio). (b) The consumption of feed stock as described by Turnover Frequency (TOF) of CO_2 (teal) and H_2 (orange) over the three catalysts indicates a considerable portion of H_2 on the monometallic Ni catalyst is wasted in the formation of CH_4 (based on reaction stoichiometric calculation). All catalysts have the same molar loading of metals, and all specific time activities are normalized to that molar amount.

the STEM characterization experiments, no crystal lattices of the NPs were observed, a result possibly suggesting structural disorder (e.g., as caused by adsorbed oxygen) or contrast limitations between the NPs and the matrix of the surrounding mesoporous support. We further examined the catalysts after activation via diffraction mode STEM measurements. These data showed no evidence of crystallinity being present within the sample.

EDX mapping confirmed that Ni and Pt atoms are uniformly distributed throughout the SBA-15 structure. Two typical sample areas are shown in Figure 2, with data shown in the STEM and EDX signal channels. The HAADF-STEM micrograph and the EDX mapping show a strong correlation between the NPs and the elemental signals; however, due to the spatial resolution, the EDX profiles appear to be conformal to the overall outline of the support. Additionally, there are no regions in which the EDX mapping indicates the presence of one metal without the other, implying that the formation of alloys/intermetallics would not be limited by segregation occurring during the impregnation/activation processes. Even so, there are some subtle differences noted between the Ni and Pt distributions within these data: some regions have somewhat higher Ni content, and the Ni shows a stronger dependence on the morphology of the silica (there are no similar correspondences for Pt that we have found). This suggests a stronger interaction between Ni and the mesoporous surfaces of the SBA-15 silicate. We note that the XAFS results presented below indicate that the NPs have a lower content of Ni compared to the stoichiometry of the full metal loading, with the excess Ni retained on the support as a silicate. We defer further comment on this point to later in the manuscript.

We evaluated the activity of the PtNi/SBA-15 catalyst system, along with controls via its monometallic analogs, using the rWGS reaction as a probe reaction. The catalytic properties of the PtNi/SBA-15 materials are presented in terms of their activity and selectivity, as quantified by measures of Specific Time Yield (STY), Turnover Frequency (TOF), and the CO/CH_4 ratio in the product effluent (Figure 3, see tabulated data in Tables S1, S2). Specific conditions used in the catalytic reaction cycles are given in the Experimental Section and SI. The hydrogenation of CO_2 generally produces two major products, CO and CH_4; the latter is the typical hydrogenation product formed over 3D-metal catalysts. The literature notes that a higher selectivity to CO is afforded by specific bimetallic catalyst compositions.[43−45] The PtNi/SBA-15 catalyst was tested along with similarly prepared and activated monometallic controls at the same (limiting) atomic loading of metal (vide supra). In the development of catalysts for the rWGS reaction, both the productivity (STY) and the selectivity of producing CO are important for evaluating performance. As shown in Figure 3a, a comparison of the productivity of the three samples suggests the catalyst with just Pt has a significantly lower activity. We carried out CO chemisorption measurements to normalize the measured activities to the samples surface area. Since Ni cannot be fully reduced by the activation conditions (vide infra), the CO chemisorption result for the Ni/SBA-15 sample may not correctly reflect the true population of active sites present in that sample. The comparison of Pt containing samples with this apparent surface area normalization indicates that the TOF of PtNi/SBA-15 is likely to have been underestimated when using a weight/molar normalization of metals. Nonetheless, our chemisorption surface area measurement justified that the activity of this catalyst is not due to a larger surface area arising from the dispersion (Table S3). Both the conversion (TOF in Figure 3b) and yield of the Pt monometallic catalyst are notably lower than those for the other two catalysts that contain Ni. One possible explanation could be that the CO and other carbon containing species produced strongly adsorb on the surface and hinder the active sites. The pure Ni loaded catalyst exhibits a much higher conversion of both reactants, but a considerable amount of H_2 (about 40% percent) is going toward the formation of CH_4 in this case. The bimetallic catalyst, PtNi/SBA-15, shows a comparable productivity of CO with the pure Ni loaded sample and has a CO/CH_4 ratio of over 195, and thus the actual selectivity is slightly better than in the pure Pt loaded catalyst (see Figure S1 for the corresponding time dependent activities).

The temperature−activity relationship reveals the impact of different structures on the activation of the reaction (Figure S2). The apparent activation energies of the rWGS reaction over the catalysts were calculated from a linear fitting of Arrhenius plots (Figure S3). The Pt monometallic catalyst has similar activation energies for CO_2 and H_2 consumption, which agrees with the activation energy calculated from the production of CO and suggests that the rWGS reaction is the dominant pathway. The PtNi bimetallic catalyst also has similar activation energies for H_2 and CO_2 consumption, though the

DOI: 10.1021/acscatal.8b00706
ACS Catal. 2018, 8, 4120−4131

values are slightly higher than those measured for the pure Pt catalyst. In contrast, the Ni monometallic catalyst, which displays a significant decrease in CO/CH_4 selectivity with increasing temperature, has a higher apparent activation energy for H_2 consumption as compared to CO_2. This difference is not one that can be meaningfully interpreted given that there is a significant and strongly temperature dependent deactivation noted within the data for this control sample. By way of comparison, there was no notable deactivation of CO production observed after more than 10 h at 673 K for either Pt-containing catalyst.

The different catalytic performances of these three catalysts, especially in their selectivity, point to an essential difference in the active site structure present in operando conditions. The key inference here is that the structure of this site for the PtNi/SBA-15 catalyst system must be associated with the metal fraction present within bimetallic NP motifs (the measured selectivity enhancements seen relative to the pure Ni/Pt controls compel this conclusion). We performed a DRIFTS study to better understand these sites using CO as the probe molecule for speciations present in the activated catalyst samples. The stretching frequency of adsorbed CO on the "on-top" sites sensitively responds to the coordination environment of the surface atoms and has been used as a useful indication of the surface structure. For metal NP catalysts, this dependence can reveal important attributes of surface characteristics, specifically the composition and alloying/segregation manifested at a NP surface. As shown in Figure 4, the spectra show

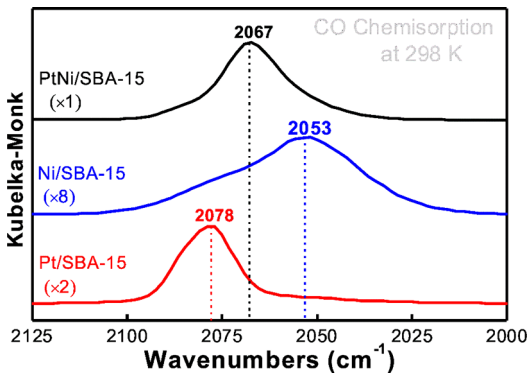

Figure 4. DRIFTS band of CO atop adsorption on metallic sites of Ni, Pt, and PtNi catalysts (after activation in H_2/673 K) recorded at 298 K with helium flow. Spectra are rescaled and with offset for plotting. The spectrum from PtNi/SBA-15 provides evidence that the CO adsorption is on an alloyed surface with the average feature between those of the two monometallic loadings.

characteristic peaks between 2000 and 2100 cm^{-1} corresponding to the stretching mode of CO molecules bound at on-top metal sites. The adsorption of CO on Ni/SBA-15 is characterized by vibrational modes dominated by an IR band at 2053 cm^{-1}. This frequency is close to the reported value assigned to a linear form of CO adsorbed on a silica-supported Ni catalyst (~2040 cm^{-1}).[46] The line shape in this case is highly asymmetric (toward higher wavenumbers), suggesting some form of structural/compositional heterogeneity is likely present (a feature of the chemistry discussed in greater detail below). For CO adsorption on the Pt/SBA-15 catalyst, due to the impact of truncated size and low coordination numbers, the vibrational frequency is significantly lower than that reported for a well-defined model single crystal substrate but matches well with values reported for supported nanometer-scale Pt clusters as well as for binding at edge/step sites.[47,48] For the PtNi/SBA-15 material, the CO stretching mode appears at 2067 cm^{-1}, a value between those seen for the most intense bands of the two monometallic catalysts. No band asymmetries/shoulder peaks of significant intensity are seen in this case. Taken together, the DRIFTS data suggest the binding of CO occurs at well-defined sites on the bimetallic catalyst that are neither Ni nor Pt dominant. This suggests attributes of structural behavior atypical of a binary alloy made from a 3D metal and Pt, which more commonly segregate Pt to the crystal surface after H_2 activation.[25] This segregation, even for the very small clusters present in this case, is expected given the 1:1 stoichiometry of Pt/Ni used in the synthesis. The nature of the compositional speciation of the NPs present in the PtNi/SBA-15 materials, and structural nature of their operando crystal truncations, are more clearly evidenced in data coming from XAS.

Figure 5 shows XAFS data measured on the Ni K-edge and the Pt L_3-edge, which together provided further information on the average valence state and local bonding characteristics (coordination numbers, bond lengths, and their disorder) of metal sites present in the operando state of the PtNi/SBA-15 catalyst. The SI Figures S4 and S5 present Extended XAFS (EXAFS) data in k-space for Ni and Pt edges, respectively. The SI Figure S6 presents the data and fits shown for the Fourier transform magnitudes and real parts. Full quantitative tabulations of the fitting of the EXAFS data are given in Table 1. As shown in Table 1, the contributions made by metal (M)−O bonding interactions are substantive for the case of Ni, for both the activated state of the PtNi/SBA-15 catalyst as well as its form under the conditions of the rWGS reaction.

In considering the broader results shown in Table 1 (most importantly, the large Ni−O coordination numbers, the importance of heterometallic (Ni−Pt) bonding, the Ni−Si scattering paths, as well the dominant contributions coming from Pt−Pt bonds), it is evident that a very specific multiphase heterogeneity must be present to account for these data, one that we believe explicitly mediates the high selectivity and activity conversions seen during the rWGS reaction. The X-ray Absorption Near Edge Structure (XANES) region of the X-ray absorption coefficient provides additional information in support of the structural model that we summarize in greater detail below. We observed marked changes in the absorption peak ("whiteline") region of both Pt and Ni during thermal activation in hydrogen.[49,50] As shown in Figure 5a, the "whiteline" peak on Ni K-edge decreases in intensity, with some subtle changes noted in other regions of the spectrum. The quantitative trends seen here are ones most consistent with speciations in which the Ni atoms have only been partially/incompletely reduced upon activation in hydrogen at 673 K. In the Fourier transformed EXAFS spectra of the Ni K edge, the most prominent feature is the peak at 1.7 Å corresponding to the Ni−O bonding. The peak amplitude decreases in the reductive conditions, in accordance with the partial reduction of Ni inferred from the XANES data, but is never completely eliminated even when the catalyst is held in a H_2 atmosphere at 673 K for 2 h. This reveals that strong interactions of Ni with the silica support must be present in some degree in the activated state of the catalyst. The spectra measured under the active conditions of the rWGS reaction show increased Ni-low Z interactions in the FT-EXAFS spectrum, compared to the previous regime (under H_2), perhaps as a consequence of a

DOI: 10.1021/acscatal.8b00706
ACS Catal. 2018, 8, 4120−4131

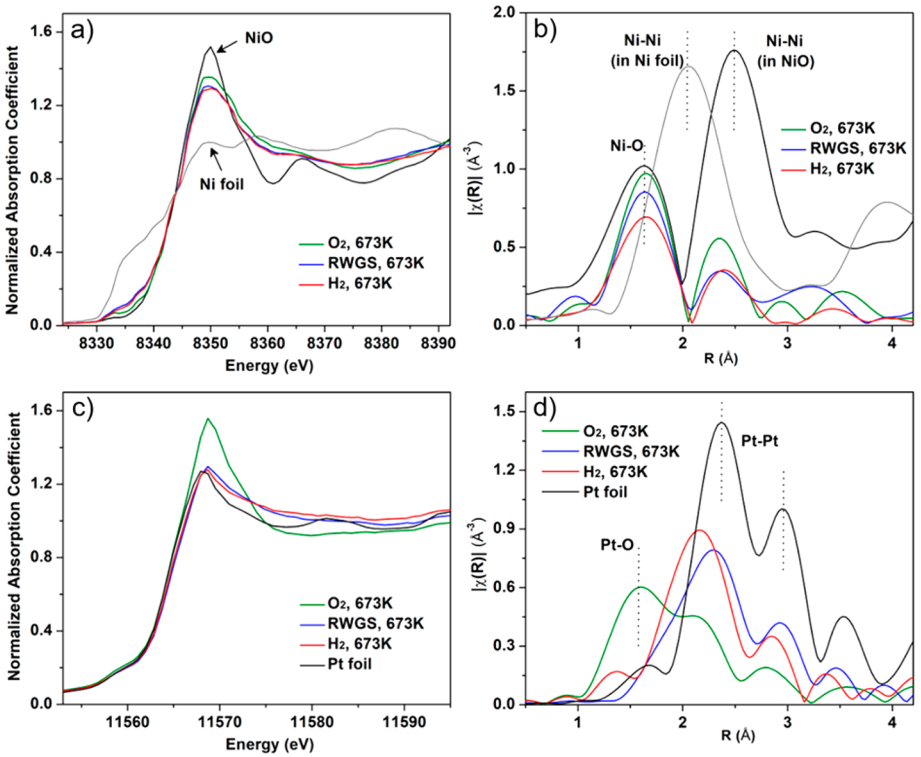

Figure 5. X-ray absorption spectroscopy (XANES and EXAFS) data measured at the (a, b) Ni K-edge and (c, d) Pt L_3-edge correspond to the speciation of the two metals on the support in the activation condition and rWGS reaction condition. Spectra from the sample in an oxidizing ambient atmosphere are also included in each panel for comparison. After the activation, the decrease in height of the main absorption peak suggests that Ni species were partially reduced while Pt was almost complete reduced. In the rWGS reaction condition, the feature of reduced metals is well-maintained. Fourier transform magnitudes of the extended X-ray absorption fine structure spectra of (b) Ni K-edge and (d) Pt L_3-edge of PtNi/SBA-15 confirm the existence of a Pt−Ni bond after reduction. Reference spectra (Pt, Ni foils, and NiO) are plotted in corresponding panels for comparison. For better comparison, the magnitudes of the R-space spectra of Ni foil and NiO were reduced by 40%, and the r-space spectrum of NiO was shifted vertically.

Table 1. EXAFS Analysis Results for PtNi/SBA-15 Catalyst under Different Gas Compositions

data	bond	N	R (Å)	σ^2 (Å^2)	ΔE (eV)
H_2 at 673 K	Ni−O	3.7 ± 0.6	2.00 ± 0.03	0.007 ± 0.002	−0.4 ± 3.0
	Ni−Pt	2.1 ± 0.8	2.60 ± 0.02	0.007 ± 0.002	−0.4 ± 3.0
	Ni−Si	2.3 ± 1.0	3.24 ± 0.05	0.007 ± 0.002	−0.4 ± 3.0
	Pt−Ni	2.1 ± 0.8	2.60 ± 0.02	0.007 ± 0.002	2.5 ± 3.3
	Pt−Pt	6.0 ± 2.2	2.65 ± 0.03	0.007 ± 0.002	2.5 ± 3.3
RWGS at 673 K	Ni−O	4.6 ± 0.8	2.00 ± 0.03	0.007 ± 0.002	−3.7 ± 3.7
	Ni−Pt	2.5 ± 0.9	2.60 ± 0.02	0.007 ± 0.002	−3.7 ± 3.7
	Ni−Si	1.7 ± 0.9	3.12 ± 0.06	0.007 ± 0.002	−3.7 ± 3.7
	Pt−Ni	2.5 ± 0.9	2.60 ± 0.02	0.007 ± 0.002	9.1 ± 3.4
	Pt−Pt	6.2 ± 2.3	2.75 ± 0.03	0.007 ± 0.002	9.1 ± 3.4

larger population of interactions occurring between Ni and C/O atoms. Considering the reduction reaction requires the adsorption of CO_2 on the catalyst surface, the differences noted may be attributed to the dissociative adsorption of CO_2 on the surface as O adatoms and carbonyl intermediates. Besides the Ni-low Z contribution, the EXAFS spectra also show a peak at about 2.4 Å, confirmed by quantitative analyses to be dominated by Ni−Pt interactions rather than Ni−Ni contributions (note, this peak is located at a distance longer than the Ni−Ni peak in Ni foil and shorter than the Ni−Ni peak in bulk NiO).

The XAFS data measured at the Ni K-edge, revealing a partially reduced state of that metal, are consistent with strong Ni−SiO_2 interactions described in the literature and a recognized feature of their chemistry.[31−34,51−53] In the synthesis of highly dispersed Ni on silica using basic conditions, it is known that Ni ions tend to share the oxygen atoms with Si−O polyhedra and, after condensation and mild dehydration, yield a stable Ni phyllosilicate. These phases (and closely analogous aluminates) require forceful conditions to fully convert base metals (e.g., Co, Ni, Mn, etc.) to silica/alumina supported clusters.[54,55] In a hydrogen atmosphere, the reduction of the metal centers in the silicates requires heating at temperatures above 750 K.[51,52] The presence of noble metals in these samples makes the reduction easier, leading to the formation of bimetallic compositions.[56] For the specific case of Ni silicates, very high reduction temperatures are required to generate fully metallic speciations (>850 K) and therefore the

DOI: 10.1021/acscatal.8b00706
ACS Catal. 2018, 8, 4120−4131

promotional effects from Pt are likely to be very important. We note that the catalysis demonstrates the importance of both Pt and Ni in the active phase of the PtNi/SBA-15 material, in full agreement with the results obtained for the Pt edge (both XANES and EXAFS).

We start the discussion of the Pt L_3-edge results with a similar overview of the Pt oxidation states and Pt-low Z bonding (Figure 5c and d). A previously activated sample of PtNi/SBA-15 oxidized in O_2 at 673 K shows an intense whiteline at about 11568 eV in Pt L_3 XANES spectrum (Figure 5c) and a significant Pt−O contribution at about 1.7 Å in the corresponding FT-EXAFS spectrum (Figure 5d). After activation in H_2 at 673 K, the intensity of the white line peak decreases markedly, with amplitudes close to that of Pt foil (a metallic state). The amplitude in the FT-EXAFS spectrum corresponding to Pt−O bonding also decrease markedly, being replaced by spectroscopic features associated with Pt−metal bond(s) (in the range of 1.6−3.2 Å). These features reveal Pt−M interactions at shorter distances compared with the Pt−Pt peak in Pt foil, a perturbation consonant both with bond strains associated with the small particle sizes present in the activated state of PtNi/SBA-15 catalyst as well as the formation of (shorter) Pt−Ni bimetallic bonds (further supporting interpretations of well-defined bimetallic habits being evidenced in DRIFTS data and in Ni edge EXAFS data). Under the active condition of the rWGS reaction, the Pt L_3-edge changes in some ways as might be associated with a more oxidized sample, notably the increase seen in the Pt "whiteline" intensity. These changes are associated with perturbations due to the adsorption of species in the operando state at Pt surface sites in the NPs (agreeing with the evidence of adsorption-based bonding changes deduced from the Ni K-edge data). The changes seen in the M−M bond distances (notably for the homometallic Pt bonds, Table 1) suggest a pronounced operando sensitivity is evidenced in the bonding states of Pt within the NPs.

The EXAFS part of the X-ray absorption spectra provides more explicit information on the atomistic features of the structural transformations discussed above. In particular, the identities of, distances to, and numbers of nearest neighbors can be quantitatively determined based on a model that includes the most important scattering paths (Table 1). We start first with a consideration of the first shell coordination numbers of the metal−metal bonding present to deduce information related the size and arrangement of atoms in the NPs.[20] To address the possibility of alloy speciations, we explicitly considered several models that include scattering paths for both homo- and heterometallic bonding of Ni and Pt atoms. The EXAFS analysis is simplified in this case in consequence of the sample characteristics revealed by the STEM data and the EDX mapping—a highly uniform spatial distribution of NPs and the likely more complex dispersion of Ni associated with its competing formation of a Ni-silicate phase (vide supra).[4,32,56] We start by noting that the signals from NP-associated (i.e., metallic) Ni atoms and those covalently bonded within the silicate phase are entwined within the ensemble average XAS data. Below, we describe an analytical model that makes it possible to quantify the Ni distribution present within this heterogeneous speciation and the atomic/electronic features of its bonding.

The method used here is one based on known bonding constraints within two limiting phases: (a) a narrow size distribution of bimetallic Pt/Ni NPs and (b) a Ni-only metal silicate. The quantitative fits show that metallic states involving homometallic Ni−Ni bonding are not present in the operando state of the PtNi/SBA-15 catalyst. As shown in Table 1, the M−M bonds are comprised predominantly of Pt−Pt and Pt−Ni bonding interactions. The known Ni−Si coordination number (4) in a pure nickel phyllosilicate (a TOT-type structure with low metal content being thermodynamically preferred after calcination)[57] allows the molar fraction of Ni present in the silicate phase to be calculated from the measured Ni−Si coordination numbers (Table 1), following a method described previously in the literature.[58] The fractions so deduced are (2.3/4) ≈ 58% and (1.7/4) ≈ 43% in the hydrogen and the rWGS regimes, respectively. The fractions of Ni atoms in the nanoparticle phases are, therefore, 42% and 57%, respectively. Given that Ni atoms in the phyllosilicate are octahedrally coordinated by oxygens atoms, the Ni−O contributions can be further differentiated, albeit qualitatively given the relative uncertainties involved, as to whether they originate from silicate or other forms of Ni (i.e., Ni-adsorbate) bonding. The latter speciations are considered in the section that follows.

The "specific" coordination numbers (N in NP), pertaining to the M−M bonds present in the NP phase, are shown in Table 2. These data reveal that the metallic bonding states are in fact quite stable (subject to only modest perturbations, in the operando conditions of the rWGS reaction). The M−O bonding states are more sensitive. Under reducing conditions (H_2/673 K), the number N_{Ni-O} in the silicate phase (6 × 58% ≈ 3.5 ± 1.5) agrees well with the overall N_{Ni-O} of 3.7 ± 0.6 (Table 1), indicating that most of the oxidized Ni atoms are in the silicate, and Ni in the NPs is predominantly reduced. The number of the Ni−O bonds in the nanoparticle in the rWGS conditions is, however, significant (as 6 × 43% ≈ 2.6 ± 1.2 is substantially smaller than the experimentally measured value of 4.6 ± 0.8, Table 1).

Table 2. Coordination Numbers of Different Pairs in Each Phase (Silicate and Nanoparticle), Given Together with the Results for the Nanoparticle Model That Gives Best Agreement with the Experimental Data[a]

regime	bond	NP (experiment)	NP (model)
H_2 at 673 K	Ni−Pt	4.9	4.8
	Pt−Ni	2.1	2.6
	Pt−Pt	6.0	5.5
rWGS at 673 K	Ni−Pt	4.3	4.8
	Pt−Ni	2.5	2.6
	Pt−Pt	6.2	5.5

[a]Experimental values for the NPs are obtained by correcting the results obtained in Table 1 by the fractions of Ni atoms in the NP phase, as described in the text.

A semiquantitative schematic model was developed to help visualize the structures deduced from the above EXAFS/XANES analyses (Figure 6). The details of the modeling are described in the Supporting Information. This model shows that the bimetallic NPs can be well described as a truncated cuboctahedron with its (111) plane attached to the support—a relatively stable and frequently seen geometric motif for supported FCC metal NPs.[36,59,60] More specifically, the model is one comprising an intermetallic structure derived from the AB_3 type stacking motif ($L1_2$) as a variation of the simple FCC structure. The composition in this model,

DOI: 10.1021/acscatal.8b00706
ACS Catal. 2018, 8, 4120−4131

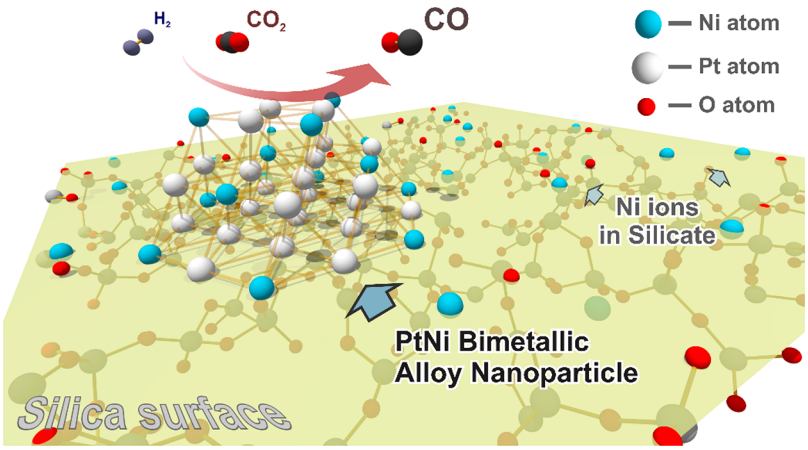

Figure 6. Schematic model of a PtNi bimetallic NP on the silica surface with unreduced Ni ions in/on silicates. The bimetallic NP consists of 37 atoms in total with platinum atoms shown in gray and nickel atoms in teal. These 25 Pt atoms and 12 Ni atoms generate an overall composition of $PtNi_{0.48}$ in the cluster without Ni−Ni bonding. The model can be regarded as a derived structure of the $L1_2$ intermetallic phase (Pt_3Ni) in the FCC lattice category. Note that 27 of 37 atoms are accessible for gas molecules, and there are only three atoms completely separated from any interfaces.

however, is not the same as that of the bulk intermetallic phase. Here, as a consequence of the finite truncation of the ∼1 nm clusters, Ni atoms reside only at the surfaces of an otherwise compact Pt core, notably occupying all of the vertex sites. In this arrangement, all Ni atoms are completely separated by Pt as is seen in the bulk structure of the Pt_3Ni intermetallic phase.[61] This impact of the cluster truncation on composition is similar to that seen and characterized for both nanometer-scale β-Pd hydride and fcc Pd_6C—atomic ratios of Pd/H or Pd/C perturbed from those comprising their bulk crystalline forms.[62,63] This model comprised of 37 atoms (12 Ni and 25 Pt), with a Ni/Pt ratio of 0.48:1, presents an atomic ratio in the intermetallic phase and a Ni content in the silicate that match very well with the experimental results. Most notably, the particle size estimated by the model ranges from 0.8 to 1.1 nm (as calculated with and without the vertex Ni), again in accordance with the characterizations made by STEM.

We tested the stiffness of the model as the best simulation for the experimental results, exploring all possible isomeric structures in the system (Figure S7 and Table S4). We screened the models with the principle constraint that direct Ni−Ni bonding interactions be excluded. The maximum possible Ni content is 13 of the 37 atoms in the ∼1 nm cluster (Figure S5, structure 0). The latter structure has the symmetry of a truncated crystalline piece of the Pt_3Ni primary cell. From this structure, other models can be derived as a series of isomeric forms with features very similar to the best-fit model (Figure 6 and Figure S8). It is possible to decrease the Ni content further and still deduce models that retain at least some of the important features seen in the experimental data (Table S5 and Figure S9). The trends seen, however, are ones that predict quantitative features of the experimental data less well (discussions of alternative models are available in the SI, section 6).

We believe the present data support a thermodynamically directed phase equilibrium that allocates Ni atoms between Ni silicate and intermetallic NPs with specific compositions. In particular, Ni phyllosilicate is very hard to reduce, and its competitive formation would drive the composition of any bimetallic clusters off of the stoichiometry used in the synthesis. The presence of Pt facilitates the reduction of at least some of the Ni in the sample.[56] All the same, this mediation appears to be limited to forming products adopting a Pt-rich (Pt_3Ni-base) intermetallic structure. It is this structure that shows the much higher activity and selectivity than either of its monometallic counterparts.

The most significant operando sensitivity seen during the rWGS feedstock is that associated with the Ni−O interactions observed for the bimetallic catalysts. The significant increases seen in this bonding post activation, after excluding the Ni−O interactions from Ni silicate moieties, demonstrate a significant sensitivity of Ni-surface sites to adsorbates formed via the dissociative adsorption of CO_2 (the reported rate-determining step) during rWGS catalysis.[17,64,65] These data, and the stable retention of the specific proportions of homometallic and heterometallic bonds in operando conditions, strongly support the qualitative features of the structural model presented in Figure 6—supported intermetallic clusters presenting a preponderance of their Ni content at the particles' interfaces. It appears most significant that, despite the strong O-adsorbate-centered interactions seen for the Ni edge of the PtNi/SBA-15 catalyst under reaction conditions, the bimetallic catalyst exhibits essentially no activity toward the formation of CH_4. The high activity and even higher selectivity of the PtNi/SBA-15 catalyst illustrate the unique nature of the active sites present in the bimetallic system relative to its homometallic comparators—a structural impact rather than a simple catalyst size/dispersion effect. The high thermodynamic stability of the Pt_3Ni intermetallic structural motif, which precludes the full conversion of Ni to a comparatively less active Ni silicate during activation, is the key constraint underpinning the selective formation of bimetallic clusters whose specific Ni−Pt surface sites mediate the dissociative adsorption of CO_2 under operando conditions.

CONCLUSIONS

In summary, we demonstrate the preparation and the characterization of a model subnanometer bimetallic catalyst with unique morphological and catalytic properties. The results demonstrate the enhanced activity and improved selectivity is associated with a specific bimetallic catalyst whose structure is related to that of a finite nanoscale truncation of a bulk parent Pt_3Ni intermetallic compound. We believe the selective formation of the latter phase is one related to thermodynamics

DOI: 10.1021/acscatal.8b00706
ACS Catal. 2018, 8, 4120−4131

of phase equilibria with a metal silicate that precludes the formation of more Ni-rich intermetallics during the operando conditions of rWGS catalysis. The proposed intermetallic structure for these ∼1 nm sized supported clusters, as illustrated schematically in Figure 6, presents a surface/interfacial speciation of the Ni in which only heterometallic Pt−Ni interactions are present—an atomic arrangement within the catalytically active bimetallic sites that affords exceptionally high activities and selectivity in catalysis.

■ ASSOCIATED CONTENT

Supporting Information

The Supporting Information is available free of charge on the ACS Publications website at DOI: 10.1021/acscatal.8b00706.

Additional facts related to the results and analysis of the activity performance tests and XAFS experiments, as well as more discussion about visualized XAFS results (PDF)

■ AUTHOR INFORMATION

Corresponding Authors

*E-mail: jgchen@columbia.edu.
*E-mail: stach@seas.upenn.edu.
*E-mail: r-nuzzo@illinois.edu.
*E-mail: frenkel@bnl.gov.

ORCID

Deyu Liu: 0000-0002-2578-9525
Daniel Grolimund: 0000-0001-9721-7940
Jingguang G. Chen: 0000-0002-9592-2635
Eric A. Stach: 0000-0002-3366-2153
Anatoly I. Frenkel: 0000-0002-5451-1207

Author Contributions

○D.Y.L. and Y.Y.L. contributed equally.

Notes

The authors declare no competing financial interest.

■ ACKNOWLEDGMENTS

The authors gratefully acknowledge support for this by the U.S. Department of Energy, Office of Basic Energy Sciences under Grant No. DE-FG02-03ER15476. DRIFTS experiments and reactivity tests were supported by the LDRD 18-047 CO/EPS grant at Brookhaven National Laboratory. The development of the microcell was supported, in part, by an LDRD grant at Brookhaven National Laboratory. The Swiss Light Source at Paul Scherrer Institute, Villigen, Switzerland, is acknowledged for provision of synchrotron radiation beamtime at the microXAS beamline. We acknowledge the facilities support provided at the Center for Functional Nanomaterials, the National Synchrotron Light Source at the Brookhaven National Laboratory (U.S. Department of Energy, Office of Basic Energy Sciences, Contract No. DE-SC0012704), and the Synchrotron Catalysis Consortium (U.S. Department of Energy, Office of Basic Energy Sciences, Grant No. DE-SC0012335).

■ REFERENCES

(1) Sinfelt, J. H. Catalysis by Alloys and Bimetallic Clusters. *Acc. Chem. Res.* **1977**, *10*, 15−20.
(2) Alonso, D. M.; Wettstein, S. G.; Dumesic, J. A. Bimetallic Catalysts for Upgrading of Biomass to Fuels and Chemicals. *Chem. Soc. Rev.* **2012**, *41*, 8075−8098.
(3) Maris, E. P.; Ketchie, W. C.; Murayama, M.; Davis, R. J. Glycerol Hydrogenolysis on Carbon-Supported Ptru and Auru Bimetallic Catalysts. *J. Catal.* **2007**, *251*, 281−294.
(4) Sankar, M.; Dimitratos, N.; Miedziak, P. J.; Wells, P. P.; Kiely, C. J.; Hutchings, G. J. Designing Bimetallic Catalysts for a Green and Sustainable Future. *Chem. Soc. Rev.* **2012**, *41*, 8099−8139.
(5) Hansgen, D. A.; Vlachos, D. G.; Chen, J. G. Using First Principles to Predict Bimetallic Catalysts for the Ammonia Decomposition Reaction. *Nat. Chem.* **2010**, *2*, 484−489.
(6) Jacobsen, C. J. H.; Dahl, S.; Clausen, B. S.; Bahn, S.; Logadottir, A.; Nørskov, J. K. Catalyst Design by Interpolation in the Periodic Table: Bimetallic Ammonia Synthesis Catalysts. *J. Am. Chem. Soc.* **2001**, *123*, 8404−8405.
(7) Zhang, J.; Teo, J.; Chen, X.; Asakura, H.; Tanaka, T.; Teramura, K.; Yan, N. A Series of Nim (M = Ru, Rh, and Pd) Bimetallic Catalysts for Effective Lignin Hydrogenolysis in Water. *ACS Catal.* **2014**, *4*, 1574−1583.
(8) Tauster, S. J.; Fung, S. C.; Baker, R. T. K.; Horsley, J. A. Strong Interactions in Supported-Metal Catalysts. *Science* **1981**, *211*, 1121.
(9) Haller, G. L.; Resasco, D. E. Metal−Support Interaction: Group Viii Metals and Reducible Oxides. *Adv. Catal.* **1989**, *36*, 173−235.
(10) Xu, J.; Froment, G. F. Methane Steam Reforming, Methanation and Water-Gas Shift: I. Intrinsic Kinetics. *AIChE J.* **1989**, *35*, 88−96.
(11) Li, Y.; Fu, Q.; Flytzani-Stephanopoulos, M. Low-Temperature Water-Gas Shift Reaction over Cu- and Ni-Loaded Cerium Oxide Catalysts. *Appl. Catal., B* **2000**, *27*, 179−191.
(12) Goguet, A.; Meunier, F. C.; Tibiletti, D.; Breen, J. P.; Burch, R. Spectrokinetic Investigation of Reverse Water-Gas-Shift Reaction Intermediates over a Pt/Ceo2 Catalyst. *J. Phys. Chem. B* **2004**, *108*, 20240−20246.
(13) Khodakov, A. Y.; Chu, W.; Fongarland, P. Advances in the Development of Novel Cobalt Fischer−Tropsch Catalysts for Synthesis of Long-Chain Hydrocarbons and Clean Fuels. *Chem. Rev.* **2007**, *107*, 1692−1744.
(14) Vance, C. K.; Bartholomew, C. H. Hydrogenation of Carbon Dioxide on Group Viii Metals: Iii, Effects of Support on Activity/Selectivity and Adsorption Properties of Nickel. *Appl. Catal.* **1983**, *7*, 169−177.
(15) Weatherbee, G. D.; Bartholomew, C. H. Hydrogenation of Co2 on Group Viii Metals: Ii. Kinetics and Mechanism of Co2 Hydrogenation on Nickel. *J. Catal.* **1982**, *77*, 460−472.
(16) Freund, H. J.; Roberts, M. W. Surface Chemistry of Carbon Dioxide. *Surf. Sci. Rep.* **1996**, *25*, 225−273.
(17) Ren, J.; Guo, H.; Yang, J.; Qin, Z.; Lin, J.; Li, Z. Insights into the Mechanisms of Co2Methanation on Ni(111) Surfaces by Density Functional Theory. *Appl. Surf. Sci.* **2015**, *351*, 504−516.
(18) Zhang, S.; Shan, J.-j.; Zhu, Y.; Frenkel, A. I.; Patlolla, A.; Huang, W.; Yoon, S. J.; Wang, L.; Yoshida, H.; Takeda, S.; Tao, F. Wgs Catalysis and in Situ Studies of Coo1−X, Ptcon/Co3o4, and Ptmcom′/Coo1−X Nanorod Catalysts. *J. Am. Chem. Soc.* **2013**, *135*, 8283−8293.
(19) Liu, X.; Wang, A.; Li, L.; Zhang, T.; Mou, C.-Y.; Lee, J.-F. Structural Changes of Au−Cu Bimetallic Catalysts in Co Oxidation. *J. Catal.* **2011**, *278*, 288−296.
(20) Frenkel, A. I. Applications of Extended X-Ray Absorption Fine-Structure Spectroscopy to Studies of Bimetallic Nanoparticle Catalysts. *Chem. Soc. Rev.* **2012**, *41*, 8163−8178.
(21) Xin, H. L.; Alayoglu, S.; Tao, R.; Genc, A.; Wang, C.-M.; Kovarik, L.; Stach, E. A.; Wang, L.-W.; Salmeron, M.; Somorjai, G. A.; Zheng, H. Revealing the Atomic Restructuring of Pt−Co Nanoparticles. *Nano Lett.* **2014**, *14*, 3203−3207.
(22) Mu, R.; Fu, Q.; Liu, H.; Tan, D.; Zhai, R.; Bao, X. Reversible Surface Structural Changes in Pt-Based Bimetallic Nanoparticles During Oxidation and Reduction Cycles. *Appl. Surf. Sci.* **2009**, *255*, 7296−7301.
(23) Hansen, P. L.; Wagner, J. B.; Helveg, S.; Rostrup-Nielsen, J. R.; Clausen, B. S.; Topsøe, H. Atom-Resolved Imaging of Dynamic Shape Changes in Supported Copper Nanocrystals. *Science* **2002**, *295*, 2053−2055.

DOI: 10.1021/acscatal.8b00706
ACS Catal. 2018, 8, 4120−4131

(24) Newton, M. A.; Belver-Coldeira, C.; Martinez-Arias, A.; Fernandez-Garcia, M. Dynamic in Situ Observation of Rapid Size and Shape Change of Supported Pd Nanoparticles During Co/No Cycling. *Nat. Mater.* **2007**, *6*, 528−532.
(25) Menning, C. A.; Chen, J. G. General Trend for Adsorbate-Induced Segregation of Subsurface Metal Atoms in Bimetallic Surfaces. *J. Chem. Phys.* **2009**, *130*, 174709.
(26) Porosoff, M. D.; Yu, W.; Chen, J. G. Challenges and Opportunities in Correlating Bimetallic Model Surfaces and Supported Catalysts. *J. Catal.* **2013**, *308*, 2−10.
(27) Mu, R.; Guo, X.; Fu, Q.; Bao, X. Oscillation of Surface Structure and Reactivity of Ptni Bimetallic Catalysts with Redox Treatments at Variable Temperatures. *J. Phys. Chem. C* **2011**, *115*, 20590−20595.
(28) Li, Y.; Zakharov, D.; Zhao, S.; Tappero, R.; Jung, U.; Elsen, A.; Baumann, P.; Nuzzo, R. G.; Stach, E. A.; Frenkel, A. I. Complex Structural Dynamics of Nanocatalysts Revealed in Operando Conditions by Correlated Imaging and Spectroscopy Probes. *Nat. Commun.* **2015**, *6*, 7583.
(29) Zhao, S.; Li, Y.; Stavitski, E.; Tappero, R.; Crowley, S.; Castaldi, M. J.; Zakharov, D. N.; Nuzzo, R. G.; Frenkel, A. I.; Stach, E. A. Operando Characterization of Catalysts through Use of a Portable Microreactor. *ChemCatChem* **2015**, *7*, 3683−3691.
(30) Marinkovic, N. S.; Wang, Q.; Frenkel, A. I. Situ Diffuse Reflectance Ir Spectroscopy and X-Ray Absorption Spectroscopy for Fast Catalytic Processes. *J. Synchrotron Radiat.* **2011**, *18*, 447−455.
(31) Yu, W.; Porosoff, M. D.; Chen, J. G. Review of Pt-Based Bimetallic Catalysis: From Model Surfaces to Supported Catalysts. *Chem. Rev.* **2012**, *112*, 5780−5817.
(32) Lonergan, W. W.; Vlachos, D. G.; Chen, J. G. Correlating Extent of Pt−Ni Bond Formation with Low-Temperature Hydrogenation of Benzene and 1,3-Butadiene over Supported Pt/Ni Bimetallic Catalysts. *J. Catal.* **2010**, *271*, 239−250.
(33) Kustov, A. L.; Frey, A. M.; Larsen, K. E.; Johannessen, T.; Nørskov, J. K.; Christensen, C. H. Co Methanation over Supported Bimetallic Ni−Fe Catalysts: From Computational Studies Towards Catalyst Optimization. *Appl. Catal., A* **2007**, *320*, 98−104.
(34) Pérez-Hernández, R.; Gutiérrez-Martínez, A.; Espinosa-Pesqueira, M. E.; Estanislao, M. L.; Palacios, J. Effect of the Bimetallic Ni/Cu Loading on the Zro2 Support for H2 Production in the Autothermal Steam Reforming of Methanol. *Catal. Today* **2015**, *250*, 166−172.
(35) Tupy, S. A.; Karim, A. M.; Bagia, C.; Deng, W.; Huang, Y.; Vlachos, D. G.; Chen, J. G. Correlating Ethylene Glycol Reforming Activity with in Situ Exafs Detection of Ni Segregation in Supported Nipt Bimetallic Catalysts. *ACS Catal.* **2012**, *2*, 2290−2296.
(36) Wu, J.; Yang, H. Synthesis and Electrocatalytic Oxygen Reduction Properties of Truncated Octahedral Pt3ni Nanoparticles. *Nano Res.* **2011**, *4*, 72−82.
(37) Benesi, H. A.; Curtis, R. M.; Studer, H. P. Preparation of Highly Dispersed Catalytic Metals. *J. Catal.* **1968**, *10*, 328−335.
(38) Cao, N.; Yang, L.; Dai, H.; Liu, T.; Su, J.; Wu, X.; Luo, W.; Cheng, G. Immobilization of Ultrafine Bimetallic Ni−Pt Nanoparticles inside the Pores of Metal−Organic Frameworks as Efficient Catalysts for Dehydrogenation of Alkaline Solution of Hydrazine. *Inorg. Chem.* **2014**, *53*, 10122−10128.
(39) He, J.; Ichinose, I.; Kunitake, T.; Nakao, A. In Situ Synthesis of Noble Metal Nanoparticles in Ultrathin Tio2−Gel Films by a Combination of Ion-Exchange and Reduction Processes. *Langmuir* **2002**, *18*, 10005−10010.
(40) Yang, C.-m.; Liu, P.-h.; Ho, Y.-f.; Chiu, C.-y.; Chao, K.-j. Highly Dispersed Metal Nanoparticles in Functionalized Sba-15. *Chem. Mater.* **2003**, *15*, 275−280.
(41) Jiao, L.; Regalbuto, J. R. The Synthesis of Highly Dispersed Noble and Base Metals on Silica Via Strong Electrostatic Adsorption: Ii. Mesoporous Silica Sba-15. *J. Catal.* **2008**, *260*, 342−350.
(42) Liu, H.; Wang, H.; Shen, J.; Sun, Y.; Liu, Z. Preparation, Characterization and Activities of the Nano-Sized Ni/Sba-15 Catalyst for Producing Cox-Free Hydrogen from Ammonia. *Appl. Catal., A* **2008**, *337*, 138−147.
(43) Porosoff, M. D.; Chen, J. G. Trends in the Catalytic Reduction of Co2 by Hydrogen over Supported Monometallic and Bimetallic Catalysts. *J. Catal.* **2013**, *301*, 30−37.
(44) Alayoglu, S.; Beaumont, S. K.; Zheng, F.; Pushkarev, V. V.; Zheng, H.; Iablokov, V.; Liu, Z.; Guo, J.; Kruse, N.; Somorjai, G. A. Co2 Hydrogenation Studies on Co and Copt Bimetallic Nanoparticles under Reaction Conditions Using Tem, Xps and Nexafs. *Top. Catal.* **2011**, *54*, 778.
(45) Kharaji, A. G.; Shariati, A.; Takassi, M. A. A Novel Γ-Alumina Supported Fe-Mo Bimetallic Catalyst for Reverse Water Gas Shift Reaction. *Chin. J. Chem. Eng.* **2013**, *21*, 1007−1014.
(46) Rochester, C. H.; Terrell, R. J. Infrared Study of Effects of Sulphur-Poisoning on the Adsorption of Carbon Monoxide by Nickel. *J. Chem. Soc., Faraday Trans. 1* **1977**, *73*, 609−621.
(47) Kappers, M. J.; van der Maas, J. H. Correlation between Co Frequency and Pt Coordination Number. A Drift Study on Supported Pt Catalysts. *Catal. Lett.* **1991**, *10*, 365−373.
(48) Raskó, J. Co-Induced Surface Structural Changes of Pt on Oxide-Supported Pt Catalysts Studied by Drifts. *J. Catal.* **2003**, *217*, 478−486.
(49) Mu, R.; Fu, Q.; Xu, H.; Zhang, H.; Huang, Y.; Jiang, Z.; Zhang, S.; Tan, D.; Bao, X. Synergetic Effect of Surface and Subsurface Ni Species at Pt−Ni Bimetallic Catalysts for Co Oxidation. *J. Am. Chem. Soc.* **2011**, *133*, 1978−1986.
(50) Boesenberg, U.; Marcus, M. A.; Shukla, A. K.; Yi, T.; McDermott, E.; Teh, P. F.; Srinivasan, M.; Moewes, A.; Cabana, J. Asymmetric Pathways in the Electrochemical Conversion Reaction of Nio as Battery Electrode with High Storage Capacity. *Sci. Rep.* **2015**, *4*, 7133.
(51) Burattin, P.; Che, M.; Louis, C. Molecular Approach to the Mechanism of Deposition−Precipitation of the Ni(Ii) Phase on Silica. *J. Phys. Chem. B* **1998**, *102*, 2722−2732.
(52) Burattin, P.; Che, M.; Louis, C. Metal Particle Size in Ni/Sio2Materials Prepared by Deposition−Precipitation: Influence of the Nature of the Ni(Ii) Phase and of Its Interaction with the Support. *J. Phys. Chem. B* **1999**, *103*, 6171−6178.
(53) Gómez-Reynoso, R.; Ramírez, J.; Nares, R.; Luna, R.; Murrieta, F. Characterization and Catalytic Activity of Ni/Sba-15, Synthesized by Deposition−Precipitation. *Catal. Today* **2005**, *107*, 926−932.
(54) Chen, L.-F.; Guo, P.-J.; Qiao, M.-H.; Yan, S.-R.; Li, H.-X.; Shen, W.; Xu, H.-L.; Fan, K.-N. Cu/Sio2 Catalysts Prepared by the Ammonia-Evaporation Method: Texture, Structure, and Catalytic Performance in Hydrogenation of Dimethyl Oxalate to Ethylene Glycol. *J. Catal.* **2008**, *257*, 172−180.
(55) Mhamdi, M.; Khaddar-Zine, S.; Ghorbel, A. Influence of the Cobalt Salt Precursors on the Cobalt Speciation and Catalytic Properties of H-Zsm-5 Modified with Cobalt by Solid-State Ion Exchange Reaction. *Appl. Catal., A* **2009**, *357*, 42−50.
(56) Wang, D.; Li, Y. Bimetallic Nanocrystals: Liquid-Phase Synthesis and Catalytic Applications. *Adv. Mater.* **2011**, *23*, 1044−1060.
(57) Che, M.; Cheng, Z. X.; Louis, C. Nucleation and Particle Growth Processes Involved in the Preparation of Silica-Supported Nickel Materials by a Two-Step Procedure. *J. Am. Chem. Soc.* **1995**, *117*, 2008−2018.
(58) Frenkel, A. Solving the 3d Structure of Metal Nanoparticles. *Z. Kristallogr. - Cryst. Mater.* **2007**, *222*, 605.
(59) Glasner, D.; Frenkel, A. I. Geometrical Characteristics of Regular Polyhedra: Application to Exafs Studies of Nanoclusters. *AIP Conf. Proc.* **2006**, *882*, 746−748.
(60) Cuenya, B. R. Synthesis and Catalytic Properties of Metal Nanoparticles: Size, Shape, Support, Composition, and Oxidation State Effects. *Thin Solid Films* **2010**, *518*, 3127−3150.
(61) Pillay, D.; Johannes, M. D. Comparison of Sulfur Interaction with Hydrogen on Pt(111), Ni(111) and Pt3ni(111) Surfaces: The Effect of Intermetallic Bonding. *Surf. Sci.* **2008**, *602*, 2752−2757.
(62) Wang, J.; Wang, Q.; Jiang, X.; Liu, Z.; Yang, W.; Frenkel, A. I. Determination of Nanoparticle Size by Measuring the Metal−Metal Bond Length: The Case of Palladium Hydride. *J. Phys. Chem. C* **2015**, *119*, 854−861.

DOI: 10.1021/acscatal.8b00706
ACS Catal. 2018, 8, 4120−4131

(63) Zhao, S.; Li, Y.; Liu, D.; Liu, J.; Liu, Y.-M.; Zakharov, D. N.; Wu, Q.; Orlov, A.; Gewirth, A. A.; Stach, E. A.; Nuzzo, R. G.; Frenkel, A. I. Multimodal Study of the Speciations and Activities of Supported Pd Catalysts During the Hydrogenation of Ethylene. *J. Phys. Chem. C* **2017**, *121*, 18962−18972.
(64) Wang, W.; Wang, S.; Ma, X.; Gong, J. Recent Advances in Catalytic Hydrogenation of Carbon Dioxide. *Chem. Soc. Rev.* **2011**, *40*, 3703−3727.
(65) Wei, W.; Jinlong, G. Methanation of Carbon Dioxide: An Overview. *Front. Chem. Sci. Eng.* **2011**, *5*, 2−10.

DOI: 10.1021/acscatal.8b00706
ACS Catal. 2018, 8, 4120−4131